JAM CM Journal of Applied Mathematics and Computational Mechanics 2026, 25(2), 139-166
www.amcm.pcz.pl p-ISSN 2299-9965
DOI: 10.17512/jamcm.2026.2.10 e-ISSN 2353-0588

ENTROPY AND SHEAR ANALYSIS OF A NON-LINEAR PERISTALTIC TRANSPORT WITH ENERGETICS PERMEABLE WALLS: MODELING ON RENAL TUBULE

***Moustafa Gouda Keshta*[1,2], *Wael Abbas*[3*], *Khaled Saad Mekheimer*[4]**
***Ali Mohamed Ali Moawad*[4]**

[1] *Basic Science Department, Canadian International College, Cairo, Egypt*
[2] *Arab East Colleges, Riyadh, Saudi Arabia*
[3] *Basic and Applied Science Department, College of Engineering and Technology, Arab Academy for Science, Technology and Maritime Transport, Cairo, Egypt*
[4] *Mathematics Department, Faculty of Science, Al-Azhar University, Nasr City (11884), Cairo, Egypt*
moustafa_gouda@cic-cairo.com, mgkeshta@arabeast.edu.sa, wael_abass@aast.edu
Kh_mekheimer@azhar.edu.eg, ali_moawad2008@azhar.edu.eg

Received: 3 March 2026; Accepted: 9 June 2026

Abstract. The study looks at how fluids move and how heat is transferred in a channel that's not symmetrical, with walls that allow fluid to pass through, and it considers the effect of a heat source or sink. This channel is created by applying a wave train with varying amplitudes and phases on the channel walls. The channel walls are kept at different temperatures and have different reabsorption coefficients. The flow of a Jeffrey fluid is studied under the assumptions of long wavelength and low Reynolds number. Due to fluid absorption through two permeable walls, the flux is taken as a function in the longitudinal axis and the tangential velocity at the walls vanishes. Approximate solutions for governing equations of the non-linear modeled system are obtained by the perturbation technique up to the second order with small wave number δ which expresses the ratio of inlet width to wavelength which giving curvature effect. Some equations are solved using numerical integration. In addition, the effect of various physical parameters such as velocity profiles, streamlines, heat transfer, entropy generation, Bejan number, Nusselt number, normal force at the wall, and wall shear stress have been analyzed and presented through graphical illustrations. Channels with permeable and reabsorping walls may be an application on renal tubule flows.

MSC 2010: *76A05, 80A20, 76W05, 80A17*
Keywords: *renal tubule, peristaltic thrusting, heat transfer, permeable walls, perturbation, tangential velocity*

1. Introduction

Urine is made in the kidneys through three main steps: glomerular filtration, tubular reabsorption, and tubular secretion. The first step, glomerular filtration, happens in the glomerulus, which is a group of tiny blood vessels inside each kidney. Blood flows through these vessels, and under pressure, water and small parts like salt, sugar,

*Corresponding author

and waste get filtered out into a sac called the Bowman's capsule. This creates a first mix of liquid that will become urine. Next, during tubular reabsorption, as this liquid moves through the kidney's tubes, most of the water and important components like sugar, amino acids, and salts are taken back into the blood through small blood vessels next to the tubes. This facilitates and maintains the balance of water and mineral salts in the human body. The final stage is tubular excretion, where excess waste, along with hydrogen, potassium, and some drugs, are transferred from the blood into the fluid through the tubules. Thus, this leads to the expulsion of unwanted substances from the human body. The essential components in the kidneys that help form urine and cleanse the blood are nephrons. Each one of them contains two essential components, known as the renal corpuscle and the renal tubule. The renal tubule is responsible for the reabsorption and excretion of substances, which are very important for the processes of urine formation and body balance. It absorbs a very large proportion of filtered substances such as glucose, amino acids, and water because of its walls are porous. Finally, the remaining filtered fluid, which consists of water, salts, urea, and uric acid, is excreted from the body as urine.

Many researchers have studied the movement of fluids in the renal tubules using mathematical models. Early work on this topic considered the tubule as a simple cylinder with a consistent shape, which made it easier to create analytical models. Macey appears to be the first person to study fluid flow in the proximal part of the renal tubule [1]. They modeled this flow as the movement of an incompressible viscous fluid through a circular tube, where the reabsorption rate along the tube wall increases linearly. Kelman [2] developed a mathematical model to describe the movement of fluid in the proximal tubule, where the flow rate decreases exponentially as the distance along the tubule increases. Macey [3] extended his initial model by incorporating Kelman's boundary condition and proceeded to solve the governing equations of motion to determine the average pressure drop. The movement of a Newtonian fluid inside a rigid, permeable tube, where fluid flows radially through the tube wall following Darcy's law, has been thoroughly examined in the study by Marshall and Trowbridge [4]. In reality, such tubes often do not maintain a uniform cross-section along their entire length, which introduces additional complexity into the modeling of flow. Radhakrishnamacharya et al. [5] carried out a comprehensive study on the hydrodynamic behavior of an incompressible viscous fluid flowing through a circular tube with a varying cross-section and reabsorption at the wall. Additionally, Chathurani and Ranganatha [6] examined how wall permeability influences velocity profiles and wall shear stress in renal tubules, representing the tubule as a tube with varying geometry. In a recent study, Muthu and Tesfahun [7] developed a mathematical model to examine the flow of a viscous, incompressible fluid through a channel that has a gradually changing cross-sectional shape and permeable walls. Both Muthu and Tesfahun demonstrated the flow of a Newtonian fluid in an irregular channel with permeable boundaries [8].

Peristalsis is a phenomenon that occurs when an expandable tube expands and contracts in a fluid, creating progressive waves that extend along the length of the

tube, mixing and moving the fluid in the direction of the waves. Also, it is a main feature found in many biological systems and is included in a unique sequence of smooth muscle movements that help move materials through hollow tubes. Fluid motion driven by peristaltic waves has been extensively investigated in both biological and mechanical systems, beginning with the foundational work of Latham [9]. Researchers have been interested in studying the basic fluid movement in peristalsis using mathematical methods, and this has helped many to understand and know how it works in both body functions and engineering applications [10–13]. For example, peristaltic motion can be used effectively in pumping sewage, sodium bromide, and sludge. Jafferin and Shapiro were among the first to introduce fundamental ideas on how to mathematically model peristaltic flows in fluid mechanics [14]. Radhakrishnamacharya investigated the motion of the fluid based on the power-law model during peristaltic flow using the assumption of the long wavelength and developed mathematical formulation that clears the behavior of the fluid [15]. The two-dimensional peristaltic flow of a Jeffery nanofluid was demonstrated in a vertically aligned channel of certain width by Lakshmi and Kavitha [16]. Elsaid conducted a theoretical study for modeling of hybrid blood Jeffrey nanofluid through the cone peristaltic artery [17]. Additionally, Channakote and Shekar investigated the peristaltic pumping of a Jeffrey model under the effect of electro-osmotic forces through a microchannel with a permeable walls [18]. Driven by advancements in medical and nanoscale fluid dynamics, recent literature extensively documents thermal and pumping investigation in biological conduits. In particular, Kumar and Tripathi evaluated the combined heat and fluid transport in a microchannel restricted by tumor growth. Adopting a different approach, the membrane driven propulsion of hybrid nanofluids, along with their heat transfer capabilities, was investigated by Kumar & Tripathi and Jangid et al. [19, 20]. Also, given its pivotal role in bio engineering, the mathematical formulation of peristaltic propulsion of non-Newtonian fluids under the effect of external magnetic fields and reactive mass transport fields has gained considerable academic traction. Recent works extensively document how fluid behavior within irregular shapes from irregular channels to asymmetric channels changes when subjected to Lorentz forces, viscous dissipation, and Newtonian heating. Ultimately, these targeted studies bridge the gap between theoretical peristalsis and its practical application in physiological processes [21–26]. Alongside these developments, the ability of nanofluids to enhance heat transfer under different conditions remains a key research topic. A key contribution in this area comes from Lin and Violi, who examined natural convection heat transfer of nanofluids in a vertical cavity. After taking into account the varying dimensions of the nanoparticles and the responsive thermal conductivity, they demonstrated that the actual distribution of the nanoparticles greatly determines the improvement in thermal performance [27].

According to thermodynamics, entropy shows how the molecules are mixed or random in a system. It is considered a tool for measuring the thermodynamic irreversibility resulting from many sources such as heat transfer, mass diffusion, and viscus dissipation. Furthermore, it has vital role in understanding the impossibility of

a system returning to its original state, a concept known as irreversibility. Therefore, both entropy and the number are considered essential factors for improving and determining energy efficiency, as well as within engineering and biomedical systems [28–31]. These factors can be applied in many industrial applications such as heat transfer, turbine machines, solar power plants, and cooling systems. Therefore, it is necessary to know the factors that reduce entropy generation and improve the efficiency of the flow system. The study of fluid flows and heat transfer within channels and tubes which are subject to different boundary conditions is one of main research fields in physics and applied mathematics. Some of researchers studied the peristaltic thrusting of a Newtonian hybrid nano fluid filled with under influences of thermal radiation, slip conditions, and entropy generation [32–34]. For non-Newtonian fluids, magnetic-caryo nanofluids were processed in peristaltic channels subjected to varying viscosity in addition to thermal conductivity [35]. Bejan et al. considered the mathematical expression for producing entropy in basic channel flow settings involving two plates, with one plate remaining stationary and the other moving. They also calculated the speed and heat transfer by using mathematics techniques, so this helped them in generating general rules for the Bejan number and entropy [36, 37]. The generation of entropy for the flow of Newtonian fluids through an inclined channel in the presence of maintaining isothermal boundary conditions was also studied by [38]. They have demonstrated that the entropy generated in a small part dominates the whole entropy generated in the entire system. Mekheimer et al. [39] studied entropy generation during the peristaltic movement of a ($Cu–Al_2O_3$) hybrid nanofluid in a flexible channel, taking into account the influence of curvature and inertial forces. We consider a Cartesian coordinate system (x^*, y^*) in a laboratory frame. The shape of the asymmetric channel is determined by setting up sinusoidal wave patterns on the top and bottom walls, each with separate amplitudes and phase differences, as shown in Figure 2. The walls of the channel are considered to be both flexible and permeable, enabling the flow of fluid through the boundaries.

$$\begin{cases} y^*(x^*,t^*) = d + h_1(x^* - ct^*), & T^* = T_u^*, \quad \text{Upper wall}, \\ y^*(x^*,t^*) = -d - h_2(x^* - ct^* + \phi), & T^* = T_l^*, \quad \text{Lower wall}. \end{cases} \tag{1}$$

In this context, d represents the half-mean width of the channel, and h_1 and h_2 are any periodic functions with different amplitudes and phases. The flow is studied in a frame that moves with the wave, traveling at the wave speed c along the channel walls. In this moving frame, the flow appears steady, provided two conditions are met: the length of the channel is an exact multiple of the wave's wavelength, and the pressure difference across the channel stays constant. The change from the stationary frame to this wave-moving frame (x, y) is described in [40, 41] by the following transformation.

$$x = x^* - ct^*, \quad y = y^*, \quad u = u^* - c, \quad v = v^*, \quad p(x,y) = p^*(x^*,y^*,t^*) \tag{2}$$

where, u, v, p, and t refer to horizontal velocity, vertical velocity, pressure, and time.

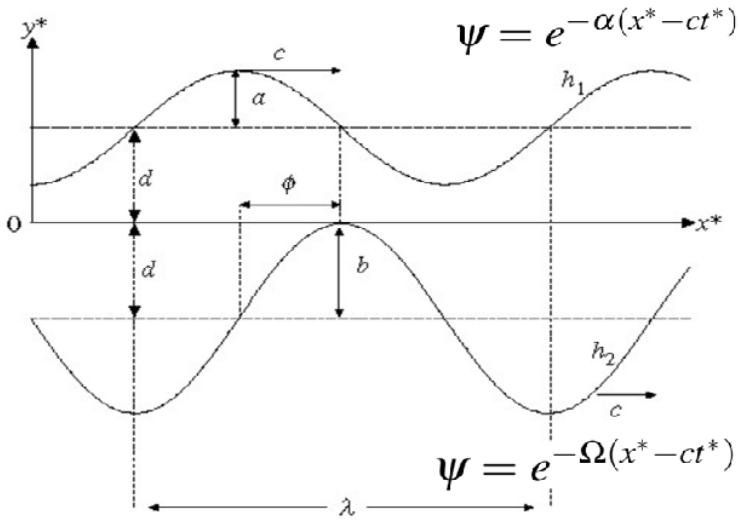

Fig. 1. The geometry of the problem

1.1. Governing equations

One of the fundamental models that describes the behavior of non-Newtonian fluids is the Jeffrey fluid. Based on a constitutive equation, it illustrates the relationship between shear stress and shear rate, taking into account both relaxation and retardation effects, which allows for a more accurate representation of viscoelasticity properties. This equation is given by [42, 43]:

$$\bar{T} = -\bar{P}\bar{I} + \bar{S} \tag{3}$$

$$\bar{S} = \frac{\mu}{1+\lambda_1}(\dot{\gamma} + \lambda_2 \ddot{\gamma}) \tag{4}$$

$$\dot{\gamma} = \nabla \mathbf{V} + (\nabla \mathbf{V})^T \tag{5}$$

In this context, $\bar{T}$ represents the Cauchy stress tensor, $\bar{S}$ is the extra or viscous stress tensor, $\bar{P}$ stands for the pressure, and $\bar{I}$ refers to the identity tensor. The symbol $\dot{\gamma}$ indicates the rate of deformation tensor, $\ddot{\gamma}$ is corresponding material time derivative, λ_1 is the ratio of relaxation to retardation times, and λ_2 denotes the relaxation time. The overdot placed above any quantity signifies differentiation with respect to time. The equations that describe the flow in a frame of reference moving at the wave speed c are obtained by applying the basic laws of mass, momentum, and energy conservation. These equations take into consideration the influence of peristaltic motion and

are simplified based on the assumptions of a long wavelength and a low Reynolds number, as shown below [18, 44]:

$$\frac{\partial u}{\partial x}+\frac{\partial v}{\partial y}=0 \tag{6}$$

$$\rho\left(u\frac{\partial u}{\partial x}+v\frac{\partial u}{\partial y}\right)=-\frac{\partial p}{\partial x}+\frac{\partial}{\partial x}\left(\frac{2\mu}{1+\lambda_1}\left(\frac{\partial u}{\partial x}+\lambda_2\left(u\frac{\partial}{\partial x}+v\frac{\partial}{\partial y}\right)\left(\frac{\partial u}{\partial x}\right)\right)\right)+\frac{\partial}{\partial y}\left(\frac{\mu}{1+\lambda_1}\left(\frac{\partial u}{\partial y}+\frac{\partial v}{\partial x}+\lambda_2\left(u\frac{\partial}{\partial x}+v\frac{\partial}{\partial y}\right)\left(\frac{\partial u}{\partial y}+\frac{\partial v}{\partial x}\right)\right)\right) \tag{7}$$

$$\rho\left(u\frac{\partial v}{\partial x}+v\frac{\partial v}{\partial y}\right)=-\frac{\partial p}{\partial y}+\frac{\partial}{\partial \bar{x}}\left(\frac{\mu}{1+\lambda_1}\left(\frac{\partial u}{\partial y}+\frac{\partial v}{\partial x}+\lambda_2\left(u\frac{\partial}{\partial x}+v\frac{\partial}{\partial y}\right)\left(\frac{\partial u}{\partial y}+\frac{\partial v}{\partial x}\right)\right)\right)+\frac{\partial}{\partial y}\left(\frac{2\mu}{1+\lambda_1}\left(\frac{\partial v}{\partial y}+\lambda_2\left(u\frac{\partial}{\partial x}+v\frac{\partial}{\partial y}\right)\left(\frac{\partial v}{\partial y}\right)\right)\right) \tag{8}$$

$$\rho c_p\left(u\frac{\partial T}{\partial x}+v\frac{\partial T}{\partial y}\right)=K\left(\frac{\partial^2 T}{\partial x^2}+\frac{\partial^2 T}{\partial y^2}\right)+h_0. \tag{9}$$

In the equations provided earlier, the terms u and v stand for the velocity components along the x and y directions, respectively, as measured in a fixed frame of reference, which is also known as the laboratory frame. The symbol ρ represents the density of the fluid, and p indicates the pressure. The variable T represents the temperature distribution, K is the thermal conductivity, h_0 is the parameter that accounts for heat generation or absorption, and c_p is the specific heat capacity of the fluid at constant pressure. The boundary conditions for flow are as follows:

1 The tangential velocity at the walls vanishes, i.e.,

$$u+\frac{d\eta_1}{dx}v=0 \quad \text{at} \quad y=\eta_1(x),$$

$$u+\frac{d\eta_2}{dx}v=0 \quad \text{at} \quad y=\eta_2(x),$$

2 The impact of fluid being reabsorbed along the walls of the channel is considered by assuming that the volume flow rate diminishes as the axial position x increases. Therefore, the flow rate through any given cross-section is described as

$$Q(x)=\int_{\eta_2(x)}^{\eta_1(x)}u(x,y)\,dy=F_0F(\Omega x),$$

When $\Omega = 0$, $F(\Omega x) = 1$, and it decreases as x increases. Ω, which is greater than or equal to zero, represents the reabsorption coefficient, and remains constant. F_0 denotes the flux through the cross-section at $x = 0$.

So, we take the stream function at the walls as follows

$$\psi(x,y) = e^{-\alpha x}, \qquad T = T_u \qquad \text{at} \quad y = \eta_1(x),$$

$$\psi(x,y) = -e^{-\Omega x}, \qquad T = T_l \qquad \text{at} \quad y = \eta_2(x).$$

where α and Ω denote the reabsorption coefficients at the lower and upper walls, respectively [8]. Now, we define the following nondimensional variables to simplify the governing equations:

$$\bar{x} = \frac{x}{\lambda}, \quad \bar{y} = \frac{y}{d}, \quad \bar{\eta_1} = \frac{\eta_1}{d}, \quad \bar{\eta_2} = \frac{\eta_2}{d}, \quad \bar{u} = \frac{d\,u}{c}, \quad \bar{v} = \frac{v\lambda}{c}, \quad \bar{p} = \frac{p\,d^2}{\mu c},$$
$$\bar{t} = \frac{ct}{\lambda}, \quad H_1 = \frac{h_1}{d}, \quad H_2 = \frac{h_2}{d}, \quad \bar{\psi} = \frac{\psi}{c}, \quad \theta = \frac{T - T_u}{T_l - T_u}$$

where λ is the wavelength, d is the characteristic height of the channel, c is the wave speed, μ is the dynamic viscosity, T is the fluid temperature, and ψ is the stream function, where

$$u = \frac{\partial \psi}{\partial y}, \quad v = -\frac{\partial \psi}{\partial x}$$

By substituting into equations (6)-(9) and omitting the bars denoting dimensionless variables, the resulting equations are obtained in simplified form as:

$$\begin{aligned} Re\,\delta\,(\psi_y\psi_{xy} - \psi_x\psi_{yy}) = {} & -\delta\,p_x + 2e_1\delta^2\psi_{xxy} \\ & + 2e_2\delta^3\,(\psi_{xy}\psi_{xxy} + \psi_y\psi_{yxxx} - \psi_{xx}\psi_{yyx} - \psi_x\psi_{yyxx}) \\ & + e_1\left(\psi_{yyy} - \delta^2\psi_{xxy}\right) \\ & + e_2\delta\Big(\psi_{yy}\psi_{xyy} + \psi_y\psi_{xyyy} - \delta^2\psi_{yy}\psi_{xxx} - \delta^2\psi_y\psi_{xxxy} \\ & \quad - \psi_{xy}\psi_{yyy} - \psi_x\psi_{yyyy} + \delta^2\psi_{xy}\psi_{xxy} + \delta^2\psi_x\psi_{xxyy}\Big) \end{aligned} \tag{10}$$

$$\begin{aligned} Re\delta^3\,(\psi_y\psi_{xx} - \psi_x\psi_{xy}) = {} & \delta\,p_y + e_1\delta^2\left(\delta^2\psi_{xxx} - \psi_{yyx}\right) \\ & + e_2\delta^3\Big(-\psi_{xy}\psi_{yyx} - \psi_y\psi_{yyxx} + \delta^2\psi_{xy}\psi_{xxx} + \delta^2\psi_y\psi_{xxxx} \\ & \quad + \psi_{xx}\psi_{yyy} + \psi_x\psi_{xyyy} - \delta^2\psi_{xx}\psi_{xxy} - \delta^2\psi_x\psi_{xxxy}\Big) \\ & + 2\delta^2 e_1\psi_{xyy} \\ & + 2\delta^3 e_2\,(\psi_{yy}\psi_{xxy} + \psi_y\psi_{xxyy} - \psi_{xy}\psi_{xyy} - \psi_x\psi_{xyyy}) \end{aligned} \tag{11}$$

$$\delta\left(\psi_y\theta_x-\psi_x\theta_y\right)=\frac{1}{Re\ Pr}\left(\delta^2\theta_{xx}+\theta_{yy}\right)+S. \tag{12}$$

Where the parameters are defined as follows: $S=\dfrac{h_0\cdot d^2}{\rho c_p c(T_l-T_u)}$ (source/sink parameter), $Pr=\dfrac{\mu\, c_p}{K}$ (Prandtl number), $\delta=\dfrac{d}{\lambda}$ (wave number), $Re=\dfrac{c\rho}{\mu}$ (Reynolds number), $e_1=\dfrac{1}{1+\lambda_1}$, and $e_2=\dfrac{c\ \lambda_2}{d^2\ (1+\lambda_1)}$. In order to convert the current model to classical viscous, we put both $e_1=1$ and $e_1=0$. Additionally, we now define the peristaltic waves on the wall using sinusoidal waves described by

$$\begin{cases}\eta_1(x)=\beta_1+\varepsilon_1\cos(2\pi x), & \theta=0, \quad \text{Upper wall},\\ \eta_2(x)=\beta_2+\varepsilon_2\cos(2\pi x+\phi), & \theta=1, \quad \text{Lower wall}.\end{cases} \tag{13}$$

2. Solution methodology

Now, we will use a perturbation technique for small wavenumber $\delta\ll 1$ to get the closed form of the approximate solution of the stream function and heat transfer. We can express ψ and θ as expansions of the following form:

$$\psi(x,y)=\sum_{n=0}^{\infty}\delta^n\psi_n(x,y),\qquad \theta(x,y)=\sum_{n=0}^{\infty}\delta^n\theta_n(x,y). \tag{14}$$

By using equation (14) in equations (10), (11), and (12), and collecting terms of equal powers for δ, we obtain the next system of partial differential equations.

Zeroth-Order System δ^0

$$\begin{cases}\psi_0^{(0,4)}(x,y)=0,\\ \\ -\theta_0^{(0,2)}(x,y)-ReSPr=0.\end{cases} \tag{15}$$

Boundary Conditions

$$\begin{cases}\psi_0^{(0,1)}(x,y)=0, \quad \psi_0(x,y)=e^{-\alpha\, x}, \quad \theta_0(x,y)=0, \quad at \quad y=\eta_1(x),\\ \psi_0^{(0,1)}(x,y)=0, \quad \psi_0(x,y)=-e^{-\Omega\, x}, \quad \theta_0(x,y)=1, \quad at \quad y=\eta_2(x).\end{cases} \tag{16}$$

First-Order System δ^1

$$\begin{cases} Re\,\psi_0^{(0,3)}(x,y)\,\psi_0^{(1,0)}(x,y) - Re\,\psi_0^{(0,1)}(x,y)\,\psi_0^{(1,2)}(x,y) + e_1\,\psi_1^{(0,4)}(x,y) \\ - e_2\,\psi_0^{(0,5)}(x,y)\,\psi_0^{(1,0)}(x,y) - 2e_2\,\psi_0^{(0,4)}(x,y)\,\psi_0^{(1,1)}(x,y) \\ + 2e_2\,\psi_0^{(0,2)}(x,y)\,\psi_0^{(1,3)}(x,y) + e_2\,\psi_0^{(0,1)}(x,y)\,\psi_0^{(1,4)}(x,y) = 0, \\ \\ -\dfrac{\theta_1^{(0,2)}(x,y)}{RePr} + \theta_0^{(1,0)}(x,y)\,\psi_0^{(0,1)}(x,y) - \theta_0^{(0,1)}(x,y)\,\psi_0^{(1,0)}(x,y) = 0. \end{cases} \tag{17}$$

Boundary Conditions

$$\begin{cases} \psi_1^{(0,1)}(x,y) = 0, \quad \psi_1(x,y) = 0, \quad \theta_1(x,y) = 0, \quad at \quad y = \eta_1(x), \\ \\ \psi_1^{(0,1)}(x,y) = 0, \quad \psi_1(x,y) = 0, \quad \theta_1(x,y) = 0, \quad at \quad y = \eta_2(x). \end{cases} \tag{18}$$

Second-Order System δ^2

$$\begin{cases} Re\Big(\psi_0^{(1,0)}(x,y)\,\psi_1^{(0,3)}(x,y) + \psi_0^{(0,3)}(x,y)\,\psi_1^{(1,0)}(x,y) \\ \quad - \psi_0^{(1,2)}(x,y)\,\psi_1^{(0,1)}(x,y) - \psi_0^{(0,1)}(x,y)\,\psi_1^{(1,2)}(x,y)\Big) \\ \quad + 2e_1\,\psi_0^{(2,2)}(x,y) + e_1\,\psi_2^{(0,4)}(x,y) \\ \quad + e_2\Big(-\psi_0^{(1,0)}(x,y)\,\psi_1^{(0,5)}(x,y) - \psi_0^{(0,5)}(x,y)\,\psi_1^{(1,0)}(x,y) \\ \qquad - 2\psi_0^{(1,1)}(x,y)\,\psi_1^{(0,4)}(x,y) - 2\psi_0^{(0,4)}(x,y)\,\psi_1^{(1,1)}(x,y) \\ \qquad + 2\psi_0^{(1,3)}(x,y)\,\psi_1^{(0,2)}(x,y) + 2\psi_0^{(0,2)}(x,y)\,\psi_1^{(1,3)}(x,y) \\ \qquad + \psi_0^{(1,4)}(x,y)\,\psi_1^{(0,1)}(x,y) + \psi_0^{(0,1)}(x,y)\,\psi_1^{(1,4)}(x,y)\Big) = 0, \\ \\ -\dfrac{\theta_0^{(2,0)}(x,y)}{RePr} - \dfrac{\theta_2^{(0,2)}(x,y)}{RePr} \\ + \theta_0^{(1,0)}(x,y)\,\psi_1^{(0,1)}(x,y) - \theta_0^{(0,1)}(x,y)\,\psi_1^{(1,0)}(x,y) \\ + \theta_1^{(1,0)}(x,y)\,\psi_0^{(0,1)}(x,y) - \theta_1^{(0,1)}(x,y)\,\psi_0^{(1,0)}(x,y) = 0. \end{cases} \tag{19}$$

Boundary Conditions

$$\begin{cases} \psi_2^{(0,1)}(x,y) = \eta_1'(x)\,\psi_0^{(1,0)}(x,y), \quad \psi_2(x,y) = 0, \quad \theta_2(x,y) = 0, \quad at \quad y = \eta_1(x), \\ \\ \psi_2^{(0,1)}(x,y) = \eta_2'(x)\,\psi_0^{(1,0)}(x,y), \quad \psi_2(x,y) = 0, \quad \theta_2(x,y) = 0, \quad at \quad y = \eta_2(x). \end{cases} \tag{20}$$

Accordingly, the solutions of the zeroth-order (δ^0), first-order (δ^1), and second--order (δ^2) approximations, which satisfy the associated boundary conditions, were obtained in closed form by using software Mathematica Wolfram 10.

3. Permeable wall mechanics and shear analysis

3.1. Permeable wall shear stress "τ" and skin friction coefficient "C_f"

Wall shear stress is the force exerted on a given area of a solid surface by a moving fluid, as well as by the fluid itself on the surface in the direction of the local tangent plane. This stress is distributed over the entire surface area and is caused by the fluid's movement. Therefore, it is a crucial parameter in fluid dynamics, especially those that focus on the analysis of viscous flows. It is considered essential and plays a vital role in calculating skin friction coefficient C_f, predicting drag forces. On the other hand, it is now clearly known that wall shear stress is necessary for keeping the endothelium healthy and for where atherosclerotic plaques form. The wall shear stress at the symmetric channel wall is given by [8, 39]:

$$\tau_w(x) = \frac{(\sigma_{yy} - \sigma_{xx})\frac{dy}{dx} + \sigma_{xy}\left[1 - \left(\frac{dy}{dx}\right)^2\right]}{1 + \left(\frac{dy}{dx}\right)^2}$$

at $y = \eta_1(x)$ and $y = \eta_2(x)$. Another physical parameter of interest in fluid flows, which is related with shear stress, is the skin friction coefficient C_f which illustrates how much drag force the fluid exerts on the wall and it is given by [45, 46]:

$$C_f = \eta(x)\left(\psi_{0yy} + \delta\,\psi_{1yy} + \delta^2\psi_{2yy}\right) + O\left(\delta^3\right).$$

3.2. Energetics of wall motion in peristaltic transport

As the fluid moves through a flexible channel via peristaltic motion, the energy needed to push the fluid forward comes from the mechanical work done by the walls of the channel. This energy is created when the wall interacts with the fluid, specifically the sideways force the fluid exerts on the wall. Since the no-slip condition means the fluid does not move along the wall, the force acting along the direction of flow

doesn't contribute to the work. Therefore, only the sideways force per unit area that the fluid applies to the wall is what actually transfers energy.

The force that pushes sideways across an area, coming from the fluid on both the top and bottom walls of the channel, is referred to as the normal stress. This force acts perpendicular to the surface and can be expressed using a mathematical equation [49]:

$$F_n = \frac{\sigma_{yy} - \sigma_{xy}\delta\frac{d\eta}{dx}}{\left(1+\delta^2\left(\frac{d\eta}{dx}\right)^2\right)^{1/2}}$$

The non-dimensional form of the normal force is written as $f = \dfrac{d^2}{\mu\, c}F_n$.

The total energy that moves between the fluid and the wall during one wave length λ is given by:

$$W = \int_0^{\lambda} \delta\frac{d}{c\mu}F_n\, dx$$

4. Thermal and irreversibility characteristics

In the study of how heat moves through convection and fluid movement, scientists use special numbers called dimensionless parameters to describe how heat is transferred and how the fluid flows. Nusselt number Nu is one of the fundamental physical numbers in thermal systems is the which explain how quickly heat is transferred by convection compared to how quickly it is transferred by conduction. This illustrates how effectively heat is transferred through the photogenic layer adjacent to the surface. Also, entropy generation has an important role in every heat transfer process because it helps minimize the system's irreversibility. The analysis of entropy is widely used in many traditional industries where fluid flow and heat is exchanged. The average Nusselt number $\overline{Nu}$ at a heated wall can be calculated using the Nusselt number as follows [39, 47].

$$\overline{\mathrm{Nu}} = -\int_0^1 \mathrm{Nu}\, dx,$$

where the Nusselt number (Nu) is given by [45, 46]

$$Nu = \eta(x)\left(\theta_{0y} + \delta\theta_{1y} + \delta^2\theta_{2y} + O\left(\delta^3\right)\right).$$

In engineering fields, entropy is generated mainly when heat is transferred between various temperatures, when fluids touch against each other, when materials are mixed, and during other processes that are not perfect [29]. In reality, the creation of entropy is linked to thermodynamic irreversibility, which is a common occurrence in every type of heat transfer system. By considering all these factors, it is possible to create energy and fluid systems that are more efficient and sustainable. We can determine

the amount of entropy produced caused by the effects of viscosity inside the fluid and at the solid surfaces as well as the irreversible nature of heat transfer as follows [39,47]:

$$E_g = \frac{k}{T_l{}^2}\left(\frac{dT}{dy}\right)^2 + \frac{\mu}{T_1}\left(\frac{du}{dy}\right)^2$$

The dimensionless entropy generation number is defined as follows:

$$N_s = \left(\frac{d\theta}{dy}\right)^2 + \frac{Br}{\omega}\left(\frac{du}{dy}\right)^2.$$

Where, $Br = \dfrac{\mu c^2}{k(T_l - T_u)}$, and $\omega = \dfrac{(T_l - T_u)}{T_l}$. Another important physical number of this study is the Bejan number Be helps us in measuring the amount of entropy produced due to the effects of viscosity inside the fluid and at the solid surfaces as well as the irreversible nature of heat transfer. It is defined by [48].

$$Be = \frac{\left(\frac{d\theta}{dy}\right)^2}{\left(\frac{d\theta}{dy}\right)^2 + \frac{Br}{\omega}\left(\frac{du}{dy}\right)^2}.$$

5. Graphical results and numerical discussion

5.1. Validation of the results

It is essential to ensure the realism and validity of the current work, with all its assumptions and results, by comparing it with previous works on the same subject. The peristalsis flow of an incompressible, steady, Newtonian fluid with an absorbing channel wall has been studied by Muthu and Berhane [8]. They included the effect of fluid being absorbed through the permeable walls by defining the wall flux based on the position along the channel. In their formulation, the channel walls were modeled according to equation (13), with the parameters set as $\beta_1 = -\beta_2 = 0.5$, $\varepsilon_1 = -\varepsilon_2 = 0.1$, and $\delta = 0.1$. Furthermore, they selected $Re = 1$ to represent flow at a low Reynolds number regime. Therefore, our results show excellent agreement with those reported in their work, validating the accuracy of our formulation. Therefore, we take $e_1 = 1$, $e_2 = 0$, $\alpha = \Omega$.

As an illustrative example, in Figure 2, we present the transverse velocity profile under the same parameter settings to demonstrate the agreement with Muthu and Berhane [8]. Also, Table 1 illustrates the numerical comparison for transverse velocity between the present study and the previous work of Muthu and Berhane [8]. The numerical values in the table illustrate that there is minimal discrepancy in the transverse velocity profiles in two cases. The results consistency of the numerical

scheme is well verified, as the absolute error is kept negligible across the grid, while the relative error never exceed permissible limits. This agreement significantly illustrates how the Newtonian flow profile emerges as a special asymptotic case of the generalized Jeffrey fluid. Therefore, the current study confirms the validity of the generalized formulation and investigates the ability to reduce to the Newtonian case under parametric requirements.

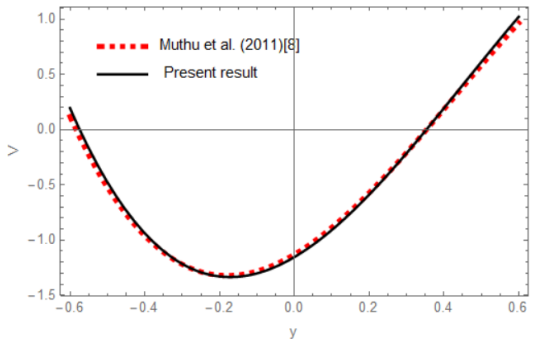

Fig. 2. Comparison of the the velocity obtained from the present study and the previous work of Muthu and Berhane [8]

Table 1. Numerical comparison of transverse velocity between Newtonian [8] and present result

y	Muthu and Berhane	Present result	Absolute Error	Relative Error
–0.5	–0.52383	–0.515819	0.008011	0.01553
–0.3	–1.21854	–1.25475	0.03621	0.02886
–0.1	–1.28066	–1.34066	0.06000	0.04475
0.0	–1.12946	–1.19368	0.06422	0.05380
0.2	–0.571091	–0.628421	0.05733	0.09123
0.7	1.30793	1.35727	0.04934	0.03636
1.0	1.90483	2.07952	0.17469	0.08401

5.2. Streamline trapping

Trapping characteristics explain how closed loops of fluid, called boluses, form and move in a peristaltic flow. These loops are created when part of the fluid gets trapped in circular areas and travels along with the wave of movement caused by the peristaltic action.

Figure 3 illustrates the streamline patterns for different values of the phase shift parameter ϕ, while keeping the other parameters fixed as $\alpha = \Omega = 0.3$, $\delta = 0.2$, $Re = 20$, $e_1 = 0.2$, and $e_2 = 0.5$. In the first Figure (a), which shows $\phi = 0$, the channel has a completely symmetrical setup with two distinct trapped boluses – one in the top half and one in the bottom half of the channel. There are closed streamline loops in both areas, showing that fluid particles are strongly trapped. The movement of the walls is symmetrical, causing similar flow recirculation above and below the centerline. This is a typical characteristic of peristaltic pumping in symmetric channels.

In the second Figure (b), when $\phi = \dfrac{\pi}{2}$, the difference in the phase between the channel walls creates a moderate imbalance in their movement, causing an uneven flow pattern. This imbalance disrupts the perfect symmetry from Case (a), leading to some fluid being trapped. The streamlines are still present but look different and have shifted from their original positions. The trapping is more noticeable in some positions than in others. Because of the phase change, ϕ affects where the fluid stalls by changing how the upper and lower walls move relative to each other, which in turn changes how the vortex and momentum are distributed in the channel. But in Case (c), when $\phi = \pi$, the situation comes to a head, causing the walls to move completely out of sync with one another. The flow is smooth and gradually increases in strength from one side of the channel to the other, indicating a clear forward direction. The walls move in opposite directions, preventing the fluid from flowing backward and therefore no fluid gets stuck in any part. This case shows that as the phase shift increases, the trapping effect gets weaker and finally disappears, changing the flow from a recirculating pattern to a simple forward-moving flow.

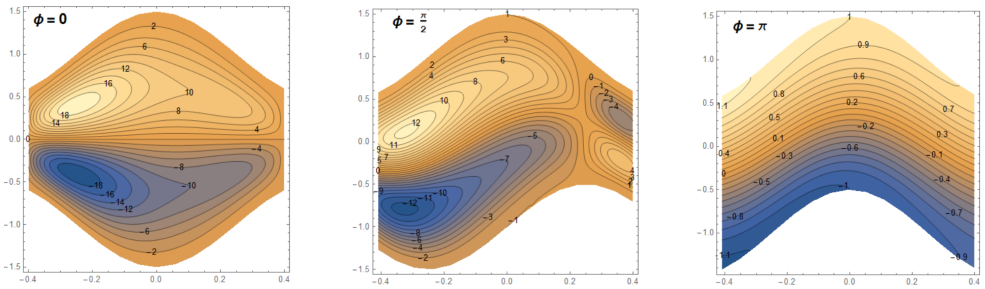

(a) Symmetric strong trapping (b) Moderate trapping (c) No trapping zones

Fig. 3. Streamline patterns under varying phase difference ϕ with varying flow parameters; $\alpha = \Omega = 0.3$, $\delta = 0.2$, $Re = 20$, $e_1 = 0.2$, $e_2 = 0.5$

Figure 4 presents the streamline patterns for varying values of the curvature effect parameter δ, while the other parameters are held constant as $\alpha = \Omega = 1$, $\phi = 0$, $Re = 20$, $e_1 = 0.2$, and $e_2 = 0.5$. In Subfigure (a), when the curvature is very small ($\delta = 0.05$), the flow lines show a nearly symmetric pattern with a small area where fluid gets trapped in the middle of the channel. The flow generally follows a straight path and is not noticeably affected by bends. The regions where the fluid is confined are of limited size, and the fluid moves at a constant pace, indicating that the behavior of the channel has little effect on the flow behavior.

In the next Figure (b), the streamlines exhibit moderate curvature ($\delta = 0.1$), resulting in a more convoluted flow pattern. This means the trapped fluid begins to swell and the flow lines become more compressed and irregular. Therefore, the flow moves in frequent circles, and the fluid becomes more stagnant. The curvature causes a noticeable change in flow, especially near the center, meaning that the shape of the walls begins to affect flow in a more significant way by creating eddies in the fluid. In the last Figure (c), the curvature is strong at ($\delta = 0.2$), and the flow pattern is

highly changed. The regions where the fluid is confined are larger and the flow lines are compact with sudden changes in velocity, also especially near the upper and lower edges. A high curvature results in a stronger vortex in the flow, leading to the confinement of a larger volume of fluid. This makes a significant difference compared to the straight flow observed in cases with less curvature.

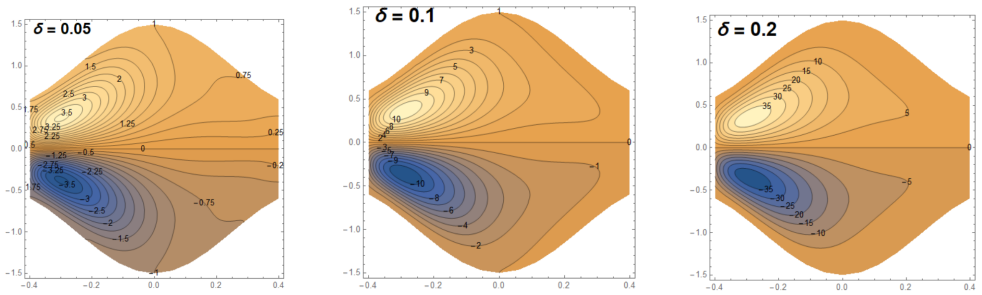

(a) Curvature effects on streamlines at $\delta = 0.05$

(b) Curvature effects on streamlines at $\delta = 0.1$

(c) Curvature effects on streamlines at $\delta = 0.2$

Fig. 4. Streamline patterns under curvature effects with varying flow parameters; $\alpha = \Omega = 1$, $\phi = 0$, $Re = 20$, $e_1 = 0.2$, $e_2 = 0.5$

Figure 5 illustrates the behavior of streamlines for peristaltic thrusting through a permeable channel that is shown using various values of related parameters α and Ω such as $0, 0.5$, and 1.0. Figure (a) shows that when $\alpha = 0$ and $\Omega = 0$, the channel walls are impermeable, resulting in symmetric trapping at both the upper and lower boundaries. These symmetrical shapes of the bolus show that the peristaltic movement is steady and consistent with permeability walls. But in the next Figure (b) at α and Ω equal 0.5, we note that there are changes in the symmetry in the streamlines pattern. The bolus in the lower part is more compact, and the vortex in the upper part is longer and narrower. But in the last Figure (c) with an increase in permeability at α and Ω becomes 1.0, in this case appears to have changed more in a streamline pattern. This means that lower part becomes tighter and more noticeable, while the upper part becomes weaker. Therefore, when the permeability is higher, more fluid is retained and the flow direction becomes unidirectional, moving mostly to the right. This shows that as the strength of the permeability impact increases, the regions where fluids are held equally on both sides become smaller and the flow direction becomes more pronounced to the right. Figure 6 illustrates the effect of inertia forces on streamlines at different levels which is expressed by the Reynolds number Re. In the first case when $Re = 0$, this means there is no inertia, so the flow lines are symmetrical around the center, resulting in the generation of smooth and closed loops that make a confined mass in the middle of the waveform. There are clear regions where the fluid flow is reversed near the upper left and lower right walls, showing that peristaltic motion is at work due to pressure and viscosity. In the second figure, when $Re = 10$, the enclosed area expands and becomes less symmetrical, moving slightly forward as the wave moves. The flow lines show higher values and the re-

verse flow or back flow regions become stronger, meaning the effect of inertia is weak against viscosity. This change shows the beginning of secondary flows near the walls, indicating the flow is becoming more complicated. At a higher *Re* of 30, inertia is the main force affecting the flow. The streamlines are very asymmetrical, and the trapped pocket moves further along with the wave and becomes more compact. The flow changes more quickly, and the backward areas are tighter, forming a small vortex. The streamlines move faster and bend more, showing that symmetry is being lost because of the inertia. Overall, as *Re* increases, the flow changes from a symmetrical, viscous-controlled flow to a more complex, inertia-driven flow with strong trapping and a more intense movement of the fluid.

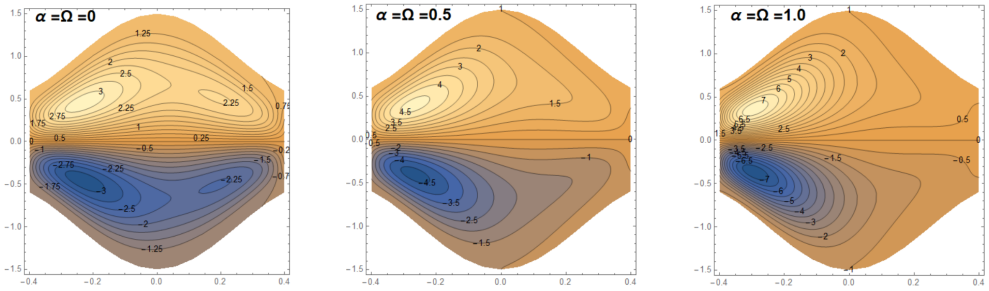

(a) Streamline patterns with no permeability effect $\alpha = \Omega = 0.0$

(b) Streamline patterns with permeability effect $\alpha = \Omega = 0.5$

(c) Streamline patterns with permeability effect $\alpha = \Omega = 1$

Fig. 5. Streamline patterns under varying wall permeability levels, represented by the parameter $\alpha = \Omega$ with varying flow parameters; $\delta = 0.0.08$, $\phi = 0$, $Re = 20$, $e_1 = 0.2$, $e_2 = 0.5$

6. Longitudinal velocity profile

Figure 7 shows six Subfigures (a–f), each displaying axial velocity (U) against vertical position (y) under different conditions. This figure explains how changes in various physical factors affect the axial velocity in a channel flow. In Case (a), the symmetry angle has a major impact on the velocity pattern, with fully asymmetric channels showing more uneven and skewed velocity profiles. But in the second Case (b), when the curvature coefficient δ becomes larger, velocity increases rapidly at the center of the channel, meaning a higher curvature leads to fast and strong flow motion. In both Subfigures (c) and (d), a gradual increase in the permeability of the upper and lower walls leads to a reduction in velocity, indicating enhanced leakage or greater flow resistance caused by the permeable channel walls. Also, Subfigure (e) illustrates the difference between Newtonian and non-Newtonian flow behaviors, with respect to non-Newtonian (Jeffrey fluid model) effects like higher viscosity and these lead to flow reversal and more complex flow patterns. But in Newtonian flow i.e., $e_1 = 1$ and $e_2 = 0$ remains more consistent. Finally, Figure (f) illustrates the impact of inertia on horizontal velocity. As the Reynolds number *Re* increases, the velocity distribution keeps consistent, mirroring the effect of inertia on trapping.

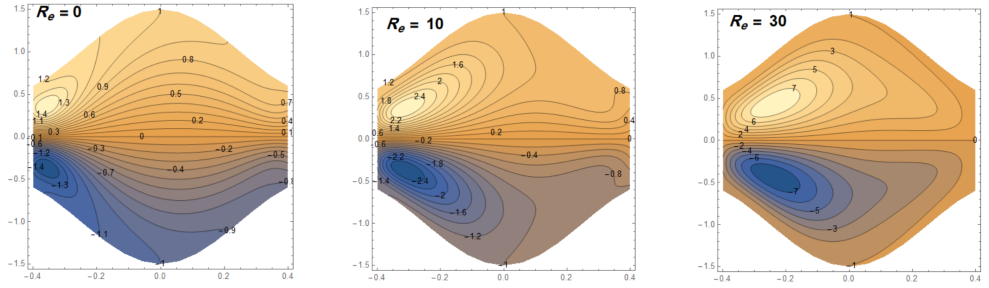

(a) Trapping with no inertia (b) Trapping with moderate inertia (c) Trapping with high inertia

Fig. 6. Streamline patterns under varying flow parameters; $\delta = 0.0.08$, $\phi = 0$, $\alpha = \Omega = 0.5$, $e_1 = 0.2$, $e_2 = 0.5$; showing the evolution of trapping zones in peristaltic transport with permeable walls

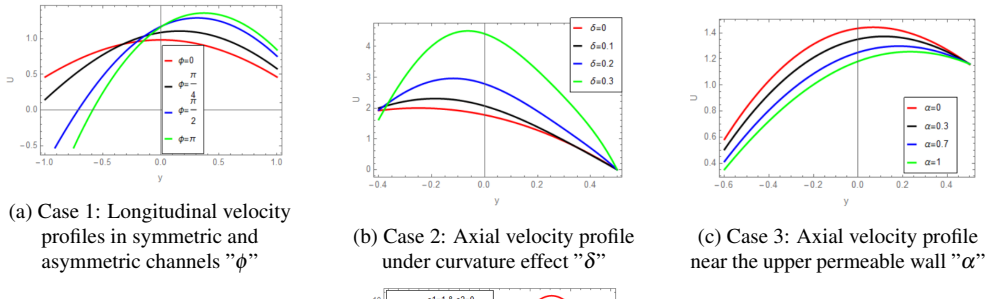

(a) Case 1: Longitudinal velocity profiles in symmetric and asymmetric channels "ϕ"

(b) Case 2: Axial velocity profile under curvature effect "δ"

(c) Case 3: Axial velocity profile near the upper permeable wall "α"

(d) Case 4: Axial velocity profile near the lower permeable wall "Ω"

(e) Case 5: Longitudinal velocity profiles in Newtonian and Non-Newtonian fluid

(f) Case 6: Inertia effects on longitudinal velocity "Re"

Fig. 7. Longitudinal velocity profiles for different values of included physical parameters

7. Transverse velocity

Figure 8 illustrates the impact of all included physical parameters on transverse velocity in current considerations. Firstly, Figure (a) shows the shape of transverse velocity profile with different values of phase shift ϕ. When the value of ϕ increases, the fluid flow becomes irregular this lead to changing the shape and direction of the transverse velocity. Terms, we can say that the transverse velocity is changing with the regularity of the channel. Additionally, the curvature effect has a clear role in transverse velocity profiles as seen in Figure (b). When the value of δ increases, the transverse velocity curve becomes deeper and more curved, and thus a more curved channel results in a stronger and more complex lateral flow. Figure (c) shows that as the value of α increases, i.e., as the amount of fluid deposited from the upper wall increases, the downward flow near the wall decreases, causing the transverse

velocity to gradually become more positive. With respect to the permeability of the lower wall shown, as seen in Figure (d), as the permeability constant increases, this coefficient slightly increases the velocity, this indicates a minor effect on the flow near the lower wall. Figure (e) illustrates the difference between the impact of viscous and Jeffry fluid on transverse velocity, here Jeffrey fluid which has higher values has more curvature and deeper motion patterns which means that the type of fluid has a significant impact on lateral flow and transverse velocity. Finally, Figure (f) illustrates how much inertia impact the flow. The figure shows that with increasing in (Re), the velocity distribution is deeper and more curved. Therefore, when there is a greater inertial force, the lateral motion becomes stronger and the flow through the channel changes more. Effects from channel symmetry (ϕ), wall permeability (α, Ω), and inertia (Re) are also important and help shape the detailed flow behavior within the channel.

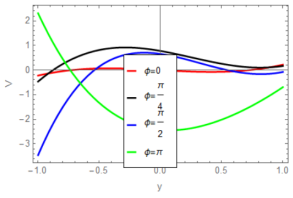

(a) Case 1: Transverse velocity with different phase shift "ϕ"

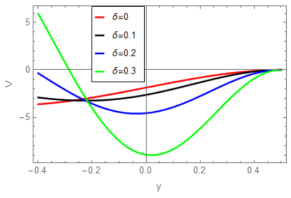

(b) Case 2: Curvature effects on Transverse velocity "δ"

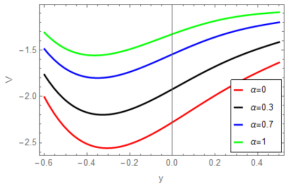

(c) Case 3: Transverse velocity profile near the upper permeable wall "α"

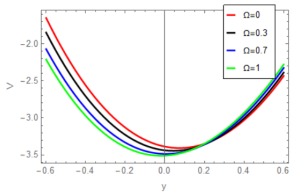

(d) Case 4: Transverse velocity profile near the lower permeable wall "Ω"

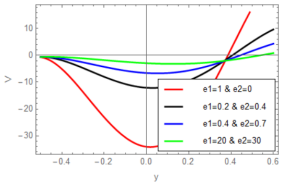

(e) Case 5: Transverse velocity in viscous and Non-Newtonian fluid

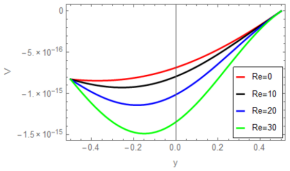

(f) Case 6: Transverse velocity under inertia effects "Re"

Fig. 8. Transverse velocity profiles under effect of serval physical parameters

8. Magnitude of wall shear stress $|\tau_w|$

Figure 9 illustrates the distribution of the magnitude of upper wall shear stress $|\tau_{w1}|$ along the axial direction x under the influence of various physical parameters.

In case 1, the reabsorption or permeability coefficient α is varied at fixed phase shift $\phi = \pi$. As α increases, the magnitude of $|\tau_w|$ decreases smoothly. This behavior suggests that higher values of α enhance the absorption or permeability through the wall, allowing more momentum to be lost from the fluid, and thereby reducing the wall shear stress. Case 2 explores the effect of the phase shift parameter ϕ on the shear stress. Variations in ϕ lead to oscillatory behavior in $|\tau_w|$, with the most

prominent peaks occurring at intermediate phase angles such as $\phi = \frac{\pi}{4}$ and $\phi = \frac{\pi}{2}$. This shows that when the oscillating force is applied at different times, it changes the flow pattern, which affects where and how the force acting on the wall is created. In Case 3, The curvature effect parameter δ is changed when $\phi = \frac{\pi}{2}$. As δ increases, the profiles become very irregular with big spikes in $|tau_w|$. This shows that wall curvature greatly affects the boundary layer, makes the wall interactions stronger, and causes areas of high shear stress because of the shape of the wall. Case 4 examines the permeability coefficient Ω, again evaluated at $\phi = \pi$. Like α, making Ω larger lowers the wall shear stress, showing a similar damping effect. The flow seems to settle down as the effects of permeability become stronger, resulting in less interaction with the walls. The figure in Case (5) illustrates the effect of Jeffrey fluid's two coefficients e_1 and e_2 on fluid flow generally. These parameters describe how quickly the fluid relaxes and decelerates. When both values of e_1 and e_2 increase, the magnitude of shear stress on the wall $|\tau_w|$ decreases steadily. Physically, this means the fluid becomes more capable of absorbing energy and reducing the force it transmits to the wall. The last figure illustrates the effect of inertia forces on shear stress in asymmetric wall channel at $\phi = \frac{\pi}{2}$. When the Reynolds number is higher, the shear stress becomes stronger and the peaks move closer to the start. This shows that the fluid's motion is more influenced by inertia. The flow becomes more powerful, causing more shear at the wall and the peaks to form earlier along the length.

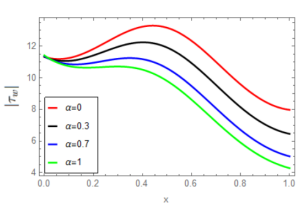

(a) Case 1: Distribution of magnitude of $|\tau_w|$ with x for α variation at $\phi = \pi$

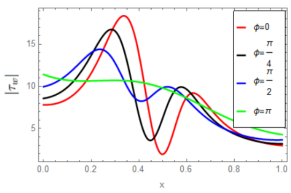

(b) Case 2: Distribution of magnitude of $|\tau_w|$ with x for ϕ variation

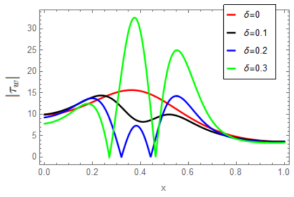

(c) Case 3: Distribution of magnitude of $|\tau_w|$ with x for δ variation at $\phi = \frac{\pi}{2}$

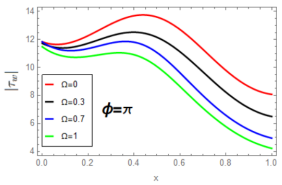

(d) Case 4: Distribution of magnitude of $|\tau_w|$ with x for Ω variation at $\phi = \pi$

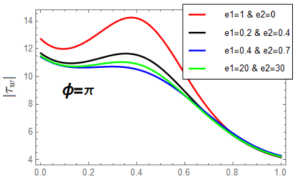

(e) Case 5: Distribution of magnitude of $|\tau_w|$ with x for Jeffrey fluid parameters $e1, e2$ at $\phi = \pi$

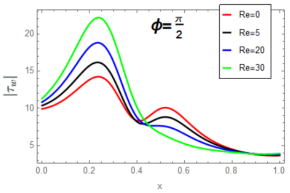

(f) Case 6: Distribution of magnitude of $|\tau_w|$ with x for Reynolds number variation at $\phi = \frac{\pi}{2}$

Fig. 9. Distribution of the magnitude of upper wall shear stress $|\tau_{w1}|$ along the axial direction (x) for various parameter values

In short, parameters like α, Ω, and the Jeffrey parameters e_1, e_2, generally lower the wall shear stress because of damping or permeability effects. In contrast, increasing δ and *Re amplifies* the shear stress through curvature-induced flow disturbances and inertial enhancement, respectively. The phase shift ϕ uniquely modulates the shear distribution in a highly dynamic and oscillatory manner, demonstrating complex temporal-spatial interactions.

9. Temperature distribution and local heat transfer rate

9.1. Temperature distribution

Figure 10 illustrates the variation in the dimensionless temperature distribution $\theta(y)$ under the influence of different physical parameters in a channel exhibiting peristaltic transport. Unlike classical forced convection problems, the present model does not rely on boundary layer approximations; instead, it captures the full velocity and thermal field as influenced by wall movement and nonlinear interactions across the entire channel.

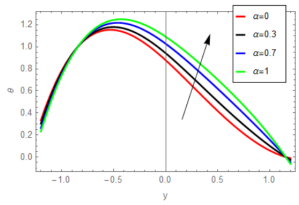

(a) Case 1: Temperature distribution with different values of permeability coefficient "α"

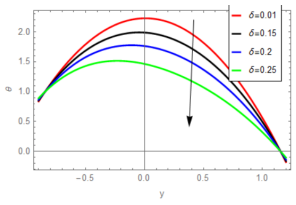

(b) Case 2: Temperature distribution under curvature effect "δ"

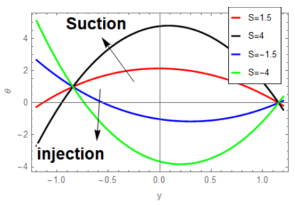

(c) Case 3:Temperature distribution under heat suction/injection effect "S"

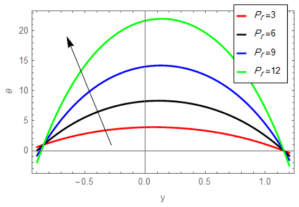

(d) Case 4:Temperature distribution under Prandtl number effect "Pr"

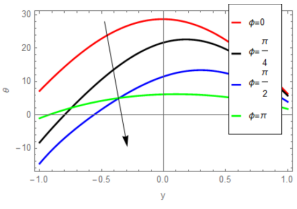

(e) Case 5: Temperature distribution in a symmetric and asymmetric channel ϕ

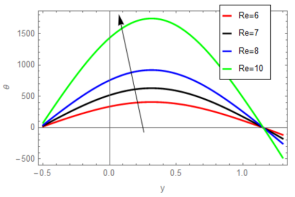

(f) Case 6:Temperature distribution under Reynolds number effect "Re"

Fig. 10. Temperature distribution for different values of physical parameters

When the permeability at the top wall α becomes larger, the temperature in the area goes up, showing that a more permeable wall allows more fluid to pass through, which helps move heat more effectively, causing higher temperatures in the fluid flow. The same thing happens when the Reynolds number Re increases, because stronger movement of the fluid (inertial forces) improves the mixing of heat and builds up more internal energy, especially in the middle part of the flow, leading to

a big increase in $\theta(y)$. Figure (b) shows the curvature effect on temperature distribution where as the parameter δ increases, the temperature decreases. Therefore, changing the geometry of the channel walls helps to mix the fluid more effectively, and it also spreads the flow along the direction of the channel and reduces hot spots. Figure (c) shows the impact of suction ($S > 0$) or injection ($S < 0$) through channel walls represented by the parameter S. At ($S > 0$), the fluid flow thrusts together and keeps heat in the central region causing in a rise in temperature. When ($S < 0$), the introduction of cooler fluid leads to a decrease in temperature.

Figure (d) illustrates the effect of Prandtl number Pr on temperature distribution. The graph shows that Pr helps improve temperature because it has less heat diffusion which in turn leads to a change in the behavior of temperature generally. When the value of ϕ increases, the temperature distribution becomes more spread out and less concentrated, which in turn disturbs the heat-transfer process because the walls move in an irregular manner.

The temperature distribution in peristaltic flow is significantly affected by factors such as permeability, curvature, fluid inertia, suction or injection, thermal diffusivity, and asymmetry of the walls. Parameters such as α, Pr, and Re intensify heat content within the channel, while higher δ, negative S, and increasing ϕ act to redistribute or reduce thermal accumulation through convective and geometric effects.

9.2. Nusselt number *Nu*

Figure 11 shows how three important physical factors permeability α, curvature δ, and Reynolds number Re affect the Nusselt number Nu. The Nusselt number measures the rate of convective heat transfer along the channel wall. Each smaller graph in the figure represents the impact of one parameter, while the other conditions remain unchanged. In Figure (a), the effect of the permeability coefficient α on the Nusselt number Nu is shown for different Prandtl numbers Pr. As α increases, the Nusselt number goes up throughout the area, and this increase is more noticeable when the Prandtl number is higher. This shows that allowing more fluid to pass through the walls improves mixing and movement of the fluid, which helps transfer heat better at the wall.

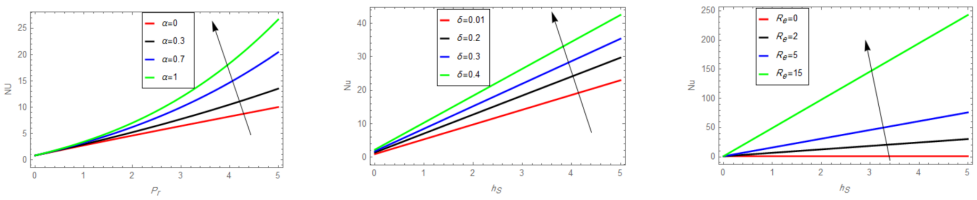

(a) The effect of permeability α on Nusselt number Nu

(b) The curvature effect δ on Nusselt number Nu

(c) The effect of inertia force on Nu

Fig. 11. The impact of different physical factors on the Nusselt number Nu

Figure (b) shows the effect of the curvature δ on pattern of Nu with heat generation S. It is observed that with an increase in the curvature of the canal's wall and

the presence of a heat source, the Nusselt number improves accordingly. The presence of the curvature effects lead to geometric deformation for the channel's wall, and this pattern causes distortion of streamlines to an additional convection movement. This distortion enhances shear and mixing, thereby improving thermal interaction between the fluid and the canal wall. Also, in Figure (c), the effect of the inertia force is shown. It is observed that inertial forces significantly influence heat transfer in fast-moving flows. This distortion enhances shear and mixing, thereby improving thermal interaction between the fluid and the canal wall. The relationship between *Re* and *Nu* is not straightforward and is much stronger.

10. Entropy generation N_s and Bejan number *Be*

Figure 12 shows how the dimensionless entropy generation N_s changes with different physical parameters in a channel where peristaltic transport occurs. In Case 1, when the Reynolds number *Re* increases from 15 to 30, N_s rises significantly, especially at higher positions along the transverse direction y, showing that inertial forces contribute to increased viscous dissipation and convective heat transfer. This is shown by the curves diverging more at larger y values, which indicates a nonlinear increase in entropy production. In Case 2, the effect of the permeability coefficient α is studied; as α goes from 0 to 1, N_s increases notably, especially in the upper part of the channel ($y > 0.5$), because higher permeability causes stronger thermal gradients and more internal flow. Figure (c) illustrates the impact of increasing *Pr* on entropy generation N_s. It is observed that as *Pr* increases, N_s rises because a higher *Pr* reduces thermal diffusion, producing steeper temperature gradients and greater entropy generation.

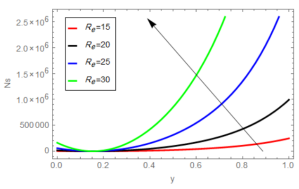

(a) Case 1: Entropy generation behavior influenced by *Re*

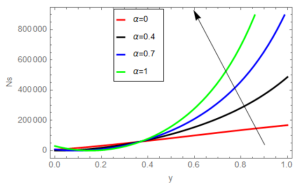

(b) Case 2: Entropy generation behavior influenced by α

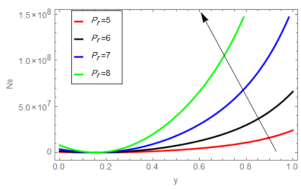

(c) Case 3: Entropy generation behavior influenced by *Pr*

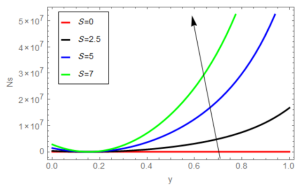

(d) Case 4: Entropy generation behavior influenced by *S*

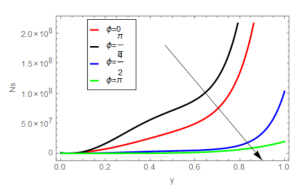

(e) Case 5: Entropy generation behavior influenced by *Re* ϕ

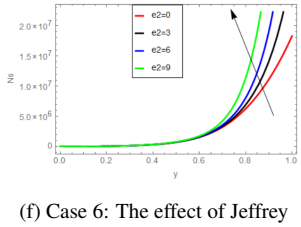

(f) Case 6: The effect of Jeffrey fluid parameter *e*2 on entropy generation

Fig. 12. The impact of different physical factors on the entropy generation N_s

In Subfigure (d), the figure shows that entropy generation is affected by the heat generation S, as S increases from 0 to 7, causing to enhancement of entropy generation N_s. Physically, that indicates that suction increases energy dissipation and leads to greater heat loss (irreversibility). Figure (e) illustrates the opposite behavior to the previous case, where changing the phase parameter ϕ leads to a decrease in entropy generation. Consequently, the geometric asymmetry induced by the phase difference reduces internal shear and heat transfer, thereby minimizing irreversibility. Finally, in Case 6, the Jeffrey fluid parameter e_2 is increased from 0 to 9, which results in higher entropy generation throughout the channel width, especially at larger y, showing that fluid relaxation effects increase internal resistance and energy dissipation.

Overall, the results reveal that parameters such as Re, α, Pr, S, and e_2 promote higher entropy generation due to stronger thermal and mechanical irreversibilities, while the phase parameter ϕ offers a potential means to control and reduce entropy in peristaltic transport systems.

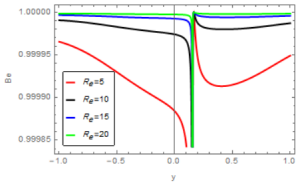

(a) Case 1: Bejan number behavior influenced by Re

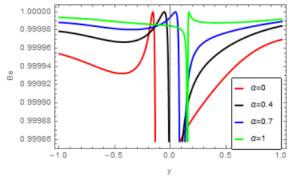

(b) Case 2: Bejan number behavior influenced by α

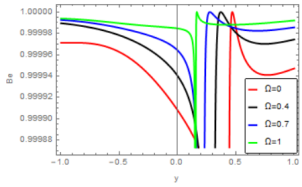

(c) Case 3: Bejan number behavior influenced by Ω

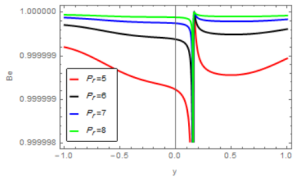

(d) Case 4: Bejan number behavior influenced by Pr

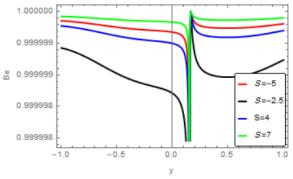

(e) Case 5: Bejan number behavior influenced by S

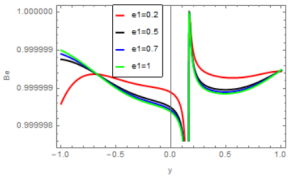

(f) Case 6: Bejan number behavior influenced by e_1

Fig. 13. Effect of various physical parameters on the Bejan number Be across the channel

Figure 13 illustrates the effect of various physical parameters on the Bejan number Be across the channel, which represents the ratio of heat transfer irreversibility to total irreversibility (i.e., the combined contribution of thermal and fluid friction irreversibilities). Values of Be close to unity indicate that entropy generation is primarily governed by heat transfer, while lower values imply increasing dominance of viscous dissipation. Figure (a) shows the effect of Re on the Bejan number Be. Near the channel centerline, Be approaches zero, but it increases progressively away from the center as Re becomes larger. Physically, this indicates that inertial effects have strengthened, increasing shear losses and fluid friction, which in turn minimizes the contribution of thermal entropy generation. Figure (b) shows the effect of upper-wall permeability α on the Bejan number Be. A similar trend is observed: higher permeability enhances fluid wall interaction and local shear, thereby increasing viscous dissipation. Also,

the permeability at the lower wall Ω is behaves similarly, since the higher values of Ω lead to localized decreases in the Bejan number at $y = 0.50$ approximately, introducing slight oscillations in the distribution and reflecting the intense frictional forces in the lower region, as shown in Figure (c). Figure (d) shows the effect of the Prandtl number Pr on the Bejan number Be. It is observed that as Pr increases from 5 to 8, the Be increases around the center of channel. This occurs because higher values of Pr reduce thermal diffusion, making temperature differences more pronounced and increasing the irreversibility associated with heat transfer relative to viscous dissipation. Figure (e) shows the effect of the heat sourcing parameter S on the Bejan number Be. It is observed that in the case of injection happens a significant minimizing in the value of Bejan number, and in the case of suction, the shape of the Began becomes flat, indicating a return to a flow dominated by heat transfer. Finally, the impact of the Jeffrey fluid parameter e_1 on Be is shown in Figure (f), when the value of e_1 increases from 0.2 to 1, where there is a significant decrease at the center of Be. This clearly illustrates the the difference between the shape of the Bejan number in Newtonian and non-Newtonian fluid.

11. Conclusions

The increase in streamlines with a higher reabsorption coefficient by approximately 2-3 times in the bolus region in the renal tubule suggests enhanced fluid transport toward the wall, indicating more efficient solute and water reabsorption under physiological conditions. The axial velocity associated with increased reabsorption and wall permeability decreases noticeably, dropping by approximately 12 % as α increases from 0 to 1 and by about 7 % as Ω increases from 0 to 1. These reductions reflect an enhanced fluid-handling capacity within the renal tubule, supporting efficient solute transport and tubular reabsorption mechanisms. Also, when the normal speed is higher than usual, it means there's more fluid moving across the cell membranes, which shows that the kidney's tubules are working harder to reabsorb fluids. The shear stress within the channel is decreasing with a higher permeability coefficient by about 21 % and when $x = 1$ occurs, the downstream value by about 45 % from $\alpha = 0$ to $\alpha = 1$, so the wall offers less resistance to fluid flow. Modifying the wall geometry to introduce a sharper channel curvature increases the surface interaction with the epithelial layer, and this structural refinement provides a promising pathway for enhancing fluid uptake. The temperature of the fluid inside the renal tubules increases by 95 % due to increased filtration or reabsorption of fluids from $\alpha = 0$ to $\alpha = 1$ when there is internal heat production due to more interaction between the fluid and the channel wall, and also less heat is removed through convection. Increased reabsorption α near the center of the channel closes the gap to unity by almost 92 %, maintaining thermal dominance as the Bejan number remains close to one. Moreover, as entropy increases, the system becomes less efficient, with more energy lost as heat or through friction. This inefficiency arises from viscous dissipa-

tion and temperature gradients within the flow. When the heat-source value is greater than zero, increasing from $S = 1.5$ to $S = 4$ raises the temperature by about 125 %, causing more heat to accumulate near the wall. In contrast, in the injection case, when $S = -1.5$ to $S = -4$, the temperature decreases by about 260 %, helping cool the region and limiting the spread of heat. Finally, the results of this work are compatible with previous research and this confirms the validity of the current model.

12. Future work

Building upon the current findings, subsequent studies might examine a wider spectrum of complex fluids to improve overall generalizability. Specifically, deploying the Carreau, Casson, and Williamson constitutive models would offer deeper insights into how varying rheological traits dictate the transport mechanisms. Casting the governing equations into cylindrical or spherical forms would significantly enhance the model's physical fidelity. Achieving higher fidelity and robust stability in these intricate nonlinear models ultimately necessitates superior discretization techniques. Consequently, transitioning toward finite element formulations, spectral methods, or elevated order finite differences represents a highly promising future direction. From a morphological perspective, substituting the current simplified boundaries with complex topographies, namely curved, tapering, or occluded sections represents a vital future step. Such structural modifications are indispensable for accurately simulating flow behaviors in intricate biological networks and advanced microfluidic devices. In order to capture the true complexity of real world physiological and industrial flows, future efforts should integrate heat transfer, MHD applications, chemical kinetics, and nanoparticle dispersion into the governing equations.

References

[1] Macey, R.I. (1963). Pressure flow patterns in a cylinder with reabsorbing walls. *The Bulletin of Mathematical Biophysics*, *25*(1), 1-9.

[2] Kelman, R.B. (1962). A theoretical note on exponential flow in the proximal part of the mammalian nephron. *The Bulletin of Mathematical Biophysics*, *24*(3), 303-317.

[3] Macey, R.I. (1965). Hydrodynamics in the renal tubule. *The Bulletin of Mathematical Biophysics*, *27*(2), 117.

[4] Marshall, E.A., & Trowbridge, E.A. (1974). Flow of a Newtonian fluid through a permeable tube: the application to the proximal renal tubule. *Bulletin of Mathematical Biology*, *36*(5), 457-476.

[5] Radhakrishnamacharya, G., Chandra, P., & Kaimal, M.R. (1981). A hydrodynamical study of the flow in renal tubules. *Bulletin of Mathematical Biology*, *43*(2), 151-163.

[6] Chaturani, P., & Ranganatha, T.R. (1991). Flow of Newtonian fluid in non-uniform tubes with variable wall permeability with application to flow in renal tubules. *Acta Mechanica*, *88*(1), 11-26.

[7] Muthu, P., & Berhane, T. (2010). Mathematical model of flow in renal tubules. *International Journal of Applied Mathematics and Mechanics*, *6*(20), 94-107.

[8] Muthu, P., & Berhane, T. (2011). Fluid flow in an asymmetric channel. *Tamkang Journal of Mathematics*, *42*, 2, 149-162.

[9] Latham, T.W. (1966). Fluid motions in a peristaltic pump (Doctoral dissertation, Massachusetts Institute of Technology).

[10] Ramachandra Rao, A., & Mishra, M. (2004). Nonlinear and curvature effects on peristaltic flow of a viscous fluid in an asymmetric channel. *Acta Mechanica*, *168*(1), 35-59.

[11] Abo-Elkhair, R.E., Mekheimer, K.S., & Moawad, A.M.A. (2019). Combine impacts of electrokinetic variable viscosity and partial slip on peristaltic MHD flow through a micro-channel. *Iranian Journal of Science and Technology, Transactions A: Science*, *43*(1), 201-212.

[12] Mohamadien, G., & El-Toukhy, F.M. (2011). The effect of thermal dispersion on unsteady MHD convective heat transfer through vertical porous. *Al-Azhar Bulletin of Science*, *2011*(12), 1-8.

[13] Kumar, A., Bhardwaj, A., & Tripathi, D. (2025). Thermal analysis in peristaltic pumping: Effects of surface roughness and channel geometries. *Physics of Fluids*, *37*(2).

[14] Jaffrin, M.Y., & Shapiro, A.H. (1971). Peristaltic pumping. *Annual Review of Fluid Mechanics*, *3*(1), 13-37.

[15] Radhakrishnamacharya, G. (1982). Long wavelength approximation to peristaltic motion of a power law fluid. *Rheologica Acta*, *21*(1), 30-35.

[16] Lakshmi, R., & Kavitha, A. (2024). Effect of suction and injection on peristaltic flow of a Jeffrey nano fluid through a vertical channel with saffman slips condition at the flexible walls. *Journal of Nanofluids*, *13*(4), 954-966.

[17] Elsaid, E.M. (2025). Simulation of blood flow in a tapered artery with ternary hybrid nanofluid and Jeffrey model. *Modern Physics Letters B*, *39*(20), 2550056.

[18] Channakote, M.M., & Shekar, M. (2024). Peristalsis of electro-osmotic Jeffrey fluid in the presence of thermal radiation and heat transfer with the permeable wall. *Jordan Journal of Mathematics and Statistics*, *17*(3).

[19] Kumar, A., & Tripathi, D. (2025). Heat transfer and flow analysis in tumor-obstructed propagating microchannel. *ASME Journal of Heat and Mass Transfer*, *147*(10), 101201.

[20] Jangid, P., Kumar, A., Tripathi, D., & Sharma, K. (2025). Heat transfer analysis in membrane-based pumping flow of hybrid nanofluids. *The European Physical Journal Plus*, *140*(2), 106.

[21] Sheikh, M., Rizwan, M., Hasnain, J., Abbas, Z., & Rafiq, M.Y. (2024). Peristaltic flow of magnetized hyperbolic tangent fluid through an asymmetric channel in the presence of homogeneous-heterogeneous reactions. *Advances in Mechanical Engineering*, *16(*12), 16878132241308929

[22] Rafiq, M.Y., Abbas, Z., Hasnain, J., & Khaliq, S. (2024). Insight into the peristaltic motion through a tapered channel with Newton's cooling subject to viscous dissipation, Lorentz force, and velocity slip. *Advances in Mechanical Engineering*, *16*(4), 16878132241241436.

[23] Abbas, Z., Shakeel, A., Rafiq, M.Y., Khaliq, S., Hasnain, J., & Nadeem, A. (2022). Rheology of peristaltic flow in couple stress fluid in an inclined tube: Heat and mass transfer analysis. *Advances in Mechanical Engineering*, *14*(11), 16878132221139984.

[24] Rafiq, M.Y., Abbas, Z., & Hasnain, J. (2021). Theoretical exploration of thermal transportation with Lorentz force for fourth-grade fluid model obeying peristaltic mechanism. *Arabian Journal for Science and Engineering*, *46*(12), 12391-12404.

[25] Abbas, Z., Rafiq, M.Y., Hasnain, J., & Umer, H. (2021). Impacts of Lorentz force and chemical reaction on peristaltic transport of Jeffrey fluid in a penetrable channel with injection/suction at walls. *Alexandria Engineering Journal*, *60*(1), 1113-1122.

[26] Abbas, Z., Rafiq, M.Y., Hasnain, J., & Javed, T. (2021). Peristaltic transport of a Casson fluid in a non-uniform inclined tube with Rosseland approximation and wall properties. *Arabian Journal for Science and Engineering*, *46*(3), 1997-2007.

[27] Lin, K.C., & Violi, A. (2010). Natural convection heat transfer of nanofluids in a vertical cavity: Effects of non-uniform particle diameter and temperature on thermal conductivity. *International Journal of Heat and Fluid Flow*, *31*(2), 236-245.

[28] Bejan, A. (1999). The method of entropy generation minimization. In Energy and the Environment (pp. 11-22). Dordrecht: Springer Netherlands.

[29] Mostapha, D.R., Nabil, T.E.D., & Abbas, W. (2024). Entropy generation and impacts of activation energy with electroosmosis of couple stresses on the peristaltic transport of Bingham blood nanofluid. *Journal of Nonlinear Mathematical Physics*, *31*(1), 86.

[30] Shawky, H.M., Eldabe, N.T., Kamel, K.A., & Abd-Aziz, E.A. (2020). Radiation effect on magnetohydrodynamic Carreau nanofluid flow past non-linear permeable heated stretching sheet with partial slip. *Al-Azhar Bulletin of Science*, *2020*(6), 1-13.

[31] Bejan, A. (1996). Entropy generation minimization: The new thermodynamics of finite-size devices and finite-time processes. *Journal of Applied Physics*, *79*(3), 1191-1218.

[32] Abbas, W., Eldabe, N.T., Abdelkhalek, R.A., Zidan, N.A., & Marzouk, S.Y. (2021). Peristaltic flow with heat transfer for nano-coupled stress fluid through non-Darcy porous medium in the presence of magnetic field. *Coatings*, *11*(8), 910.

[33] Soliman, H. A. (2022). New investigation of asymmetric wall temperature and fluid-wall interaction on radiative steady MHD fully developed natural convection in vertical micro-porous--channel. *Al-Azhar Bulletin of Science*, *33*(2-B), 45-58.

[34] Farooq, S., Khan, M.I., Waqas, M., Hayat, T., & Alsaedi, A. (2020). Transport of hybrid type nanomaterials in peristaltic activity of viscous fluid considering nonlinear radiation, entropy optimization and slip effects. *Computer Methods and Programs in Biomedicine*, *184*, 105086.

[35] Khan, W.A., Farooq, S., Kadry, S., Hanif, M., Iftikhar, F.J., & Abbas, S.Z. (2020). Variable characteristics of viscosity and thermal conductivity in peristalsis of magneto-Carreau nanoliquid with heat transfer irreversibilities. *Computer Methods and Programs in Biomedicine*, *190*, 105355.

[36] Mahmud, S., & Fraser, R.A. (2002). Thermodynamic analysis of flow and heat transfer inside channel with two parallel plates. *Exergy, an International Journal*, *2*(3), 140-146.

[37] Mahmud, S., & Fraser, R.A. (2003). The second law analysis in fundamental convective heat transfer problems. *International Journal of Thermal Sciences*, *42*(2), 177-186.

[38] Havzali, M., Arikoglu, A., Komurgoz, G., Keser, H.I., & Ozkol, I. (2008). Analytical-numerical analysis of entropy generation for gravity-driven inclined channel flow with initial transition and entrance effects. *Physica Scripta*, *78*(4), 045401.

[39] Mekheimer, K.S., Abo-Elkhair, R.E., Ali, K.K., & Keshta, M.G. (2021). Entropy generation and curvature effect on peristaltic thrusting of ($Cu–Al_2O_3$) hybrid nanofluid in resilient channel: Nonlinear analysis. *Heat Transfer*, *50*(8), 7918-7948.

[40] Abbas, W., Eldabe, N., Abdelkhalek, R., Zidan, N., & Marzouk, S. (2021). Soret and Dufour effects with Hall currents on peristaltic flow of Casson fluid with heat and mass transfer through non-Darcy porous medium inside vertical channel. *Egyptian Journal of Chemistry*, *64*(9), 5215-5225.

[41] Abo-Elkhair, R.E., Mekheimer, K.S., & Moawad, A.M.A. (2017). Cilia walls influence on peristaltically induced motion of magneto-fluid through a porous medium at moderate Reynolds number: Numerical study. *Journal of the Egyptian Mathematical Society*, *25*(2), 238-251.

[42] Mekheimer, K.S., & Abo-Elkhair, R.E. (2018). Lie point symmetries for biological magneto--Jeffrey fluid flow in expanding or contracting permeable walls: a blood vessel model. *Journal of Taibah University for Science*, *12*(6), 738-747.

[43] Mekheimer, K.S., Abo-Elkhair, R.E., & Moawad, A.M.A. (2018). Electro-osmotic flow of non--Newtonian biofluids through wavy micro-concentric tubes. *BioNanoScience*, *8*(3), 723-734.

[44] Rehman, M., Noreen, S., Haider, A., & Azam, H. (2015). Effect of heat sink/source on peristaltic flow of Jeffrey fluid through a symmetric channel. *Alexandria Engineering Journal*, *54*(3), 733-743.

[45] Imran, N., Javed, M., Sohail, M., & Tlili, I. (2020). Simultaneous effects of heterogeneous--homogeneous reactions in peristaltic flow comprising thermal radiation: Rabinowitsch fluid model. *Journal of Materials Research and Technology*, *9*(3), 3520-3529.

[46] Makinde, O.D., Gnaneswara Reddy, M., & Venugopal Reddy, K. (2017). Effects of thermal radiation on MHD peristaltic motion of Walters-B fluid with heat source and slip conditions. *Journal of Applied Fluid Mechanics*, *10*(4), 1105-1112.

[47] Nagarajan, N., & Akbar, S. (2015). Heat transfer enhancement of Cu-water nanofluid in a porous square enclosure driven by an incessantly moving flat plate. *Procedia Engineering*, *127*, 279-286.

[48] Keshta, M.G., Mekheimer, K.S., Abo-Elkhair, R.E., & Ali, K.K. (2024). Irreversibility of heat transfer with the curvature effect on peristaltic thrusting of micropolar fluid in a resilient channel in the presence of heat generation: Nonlinear analysis. *International Journal of Ambient Energy*, *45*(1), 2280218.

[49] Manton, M.J. (1975). Long-wavelength peristaltic pumping at low Reynolds number. *Journal of Fluid Mechanics*, *68*(3), 467-476.